

## Direct measurements of cosmic rays using balloon borne experiments

E.S. Seo\*

*Institute for Physical Science and Technology, University of Maryland, College Park, MD 20742, USA*

### ARTICLE INFO

#### Article history:

Available online 17 April 2012

#### Keywords:

Cosmic rays  
Particle acceleration  
Cosmic ray propagation  
Cosmic ray origin  
Balloons

### ABSTRACT

Direct measurements of cosmic rays with balloon-borne detectors are used for understanding cosmic ray origin, acceleration and propagation, as well as exploring the supernova acceleration limit and searching for exotic sources such as dark matter. The energy reach of direct measurements is currently limited to  $\sim 10^{15}$  eV by the detector size and exposure time, but incident particles are identified element-by-element with excellent charge resolution. A challenge of balloon-borne experiments is that the detectors must be large enough to collect adequate statistics, yet stay within the weight limit available for balloon flight. Innovative approaches now promise high quality measurements over an energy range that was not previously possible. Recent results and their implications are reviewed. The outlook of existing and future experiments is also discussed.

© 2012 Elsevier B.V. All rights reserved.

### 1. Scientific ballooning

Cosmic rays were discovered in 1912 with the use of a balloon manned by Victor Hess. His balloon ascended to only  $\sim 5$  km, but it was found that the ionization rate increased at the high altitude, indicating that the radiation came not from Earth but rather from space.

In the early 1930s stratospheric flights were made with huge rubberized fabric balloons. Aeronauts in sealed, air-tight capsules were able to survive to  $\sim 18$  km. The altitude record of 22 km set in 1935 by U.S. Army Captains Stevens and Anderson in Explorer II stood for 12 years implying a limit for rubberized balloons. Scientific balloon payloads have been flown for periods of 1–2 days since large polyethylene balloons were first introduced in the 1950s. The conventional balloons used today by NASA have changed only incrementally since those early days [1].

Conventional balloons are made of 20  $\mu\text{m}$  thick polyethylene film, and they are as large as a football stadium with a diameter of  $\sim 140$  m and a volume of  $\sim 1.12$  million cubic meters (MCM). They are filled with helium gas, and vented at the bottom to keep zero pressure difference with the surrounding atmosphere. Balloons are only partially inflated when launched, and they fill up with the decreasing atmospheric pressure until they are fully inflated. They can carry payloads up to 3600 kg and fly at altitudes up to 42 km. The bottom of the balloon is attached to a parachute, from which the payload is attached with steel suspension cables, as shown in Fig. 1(a). A flight is terminated by remotely firing an explosive squib that separates the parachute from the balloon. A rip line simultaneously tears open the top of the balloon, which

quickly deflates and falls to the ground, to be recovered and discarded after a single use. The payload descends slowly, suspended by the parachute, and is recovered by the ground crew. Many, if not most payloads are refurbished for future flights.

The launch of a large balloon requires conjunction of light low-level winds, to comply with limitations of the dynamic launch technique, and suitable upper-level winds. The balloon must remain within telemetry range of a ground station until it reaches its float altitude, and subsequently stay within the permitted flight region. A payload may be rolled out to the launch area several times before surface and upper atmosphere conditions are acceptable for launch. During the flight, data are transmitted to the ground for analysis, and command uplink allows active control of payloads. Usually data are also recorded on-board.

Significant changes in ballooning capability occurred with the inauguration of 1–2 week long flights around Antarctica in the early 1990s. These long duration balloon (LDB) flights employ zero-pressure polyethylene balloons identical to those utilized for conventional 1–2 day flights, whose durations are limited due to altitude excursions during day-night transitions. The order of magnitude improvement in flight duration in the polar region is possible because of constant daylight during local summer. The continuous solar heating ensures nearly constant altitudes with essentially no ballasting. These circumpolar flights have been remarkably successful, with many investigations utilizing multiple flights of payloads that are recovered, refurbished, and re-flown. In 2005, a new LDB flight record was set when the cosmic ray energetic and mass (CREAM) payload flew for  $\sim 42$  days while circumnavigating the continent three times [2]. This payload has accumulated  $\sim 161$  days of exposure in six flights, which is the longest duration for a single balloon project. See Fig. 1(b) for an example of a flight trajectory in Antarctica. With exposure factors

\* Tel.: +1 301 405 4855.

E-mail address: [seo@umd.edu](mailto:seo@umd.edu)



**Fig. 1.** (a) CREAM ballooncraft with the launch vehicle while a  $\sim 1$  MCM balloon is being inflated at the launch site, Williams field near McMurdo, Antarctica; (b) Balloon trajectory of a 37 day flight of CREAM, which was launched on December 1, 2009 and terminated on January 8, 2010 during about 3 rounds of the South Pole.

larger than those in previous years, recent experiments have yielded unprecedented observations of cosmic rays over a wide range of energies and species. These new results address key physics of cosmic ray origin, acceleration, and propagation.

## 2. Searches for antimatter and dark matter

The Galactic halo may not be as empty as it appears, but rather filled with weakly interacting massive particles (WIMPs) like the neutralino, a dark matter candidate. When neutralinos interact they would behave like their own antiparticle to annihilate and produce normal particles, such as electrons and positrons. A contribution from dark matter annihilation would appear as an excess flux in the positron, antiproton, anti-deuteron, and/or gamma-ray spectra predicted by conventional cosmic ray propagation models (e.g. 3).

The balloon experiment with a superconducting spectrometer (BESS) and other prior balloon payloads, like the cosmic anti-particle ring imaging Cherenkov experiment (CAPRICE) and the high energy antimatter telescope (HEAT), employ superconducting magnets with a suite of particle detectors to identify antiparticles. Being exactly the same as particles except for their opposite charge sign, antiparticles are readily distinguished as they bend in opposite directions in the magnetic field. See Fig. 2a for the BESS instrument cross sectional view, which illustrates a negative particle

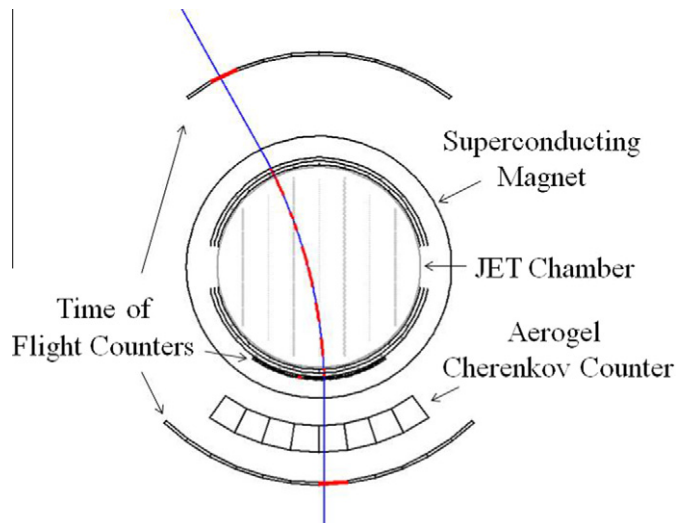


**Fig. 2a.** A cross sectional view of the BESS instrument with a particle trajectory.

trajectory. Fig. 2b illustrates how well different particles are separated in BESS. Particles with positive rigidity and positive beta are downward moving positive particles, i.e., low mass  $Z = 1$  particles (electrons, muons, and pions), protons, deuterons and tritium from the top band to the bottom. Particles with negative rigidity and positive beta are downward moving negative particles. The low mass particle band is clear, showing no antiproton in this small sample of data. Particles with negative beta, i.e., albedo protons and low mass particles, are also clearly shown.

BESS had nine conventional  $\sim 1$ -day balloon flights in Canada and the U.S. between 1993 and 2002 with the objective of measuring the spectra of light nuclei, including anti-particles. An 8-1/2 day Antarctic flight carried out in 2004 and a 30-day flight launched in 2007 continued the search for a possible exotic matter signature in low-energy antiproton data. The low geomagnetic cut-off in the polar region extended antiproton measurements to lower energies, and the long duration flights increased the statistics significantly. Most of the existing antiproton data come from BESS, which has not shown any features, implying that the observed antiprotons are secondaries produced by cosmic ray interactions with the interstellar medium.

These magnet spectrometers simultaneously probe the existence of antimatter. Equal amounts of matter and antimatter were produced at the beginning of the universe as described by the Big Bang scenario, but there now seems to be only matter around us.

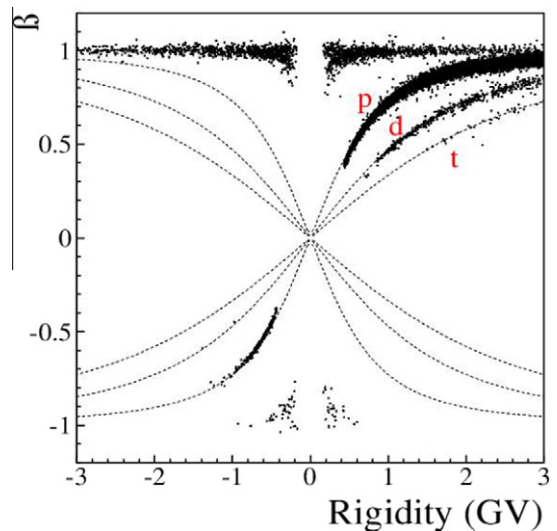


**Fig. 2b.** A scatter plot of beta vs rigidity showing bands of particles with different charge sign, velocity and mass. Dotted curves represent particles with proton, deuteron and tritium mass.

The possible presence of cosmological antimatter and the nature of dark matter in the universe are fundamental physics issues. The detection of one antihelium or anticarbon nucleus would impact our understanding of the origin of symmetry in time, which is the foundation of modern physics. BESS provides the lowest upper limit to date on the relative antihelium-to-helium ratio,  $6.9 \times 10^{-8}$ , in the rigidity range 1–14 GV [4]. BESS also provides the lowest upper limit antideuteron flux  $1.9 \times 10^{-4} (\text{m}^2\text{-s-sr-GeV/n})^{-1}$  at the 95% confidence level, between 0.17 and 1.15 GeV/n [5].

A more sensitive search for lower energy anti-deuterons is planned with the balloon-borne general antiparticle spectrometer (GAPS). Secondary anti-deuterons, like antiprotons, are produced through cosmic-ray interactions with the interstellar medium. However, this probability is very low and the low energy search for primary anti-deuterons is essentially background-free. The detection of a single anti-deuteron would be, in principle, a signature of dark matter. The GAPS approach involves capturing anti-deuterons in the Si (Li) target, where an “exotic” atom is formed. A unique detection signature would appear when the exotic atom decays with the emission of both X-rays and pions. With high sensitivity, GAPS can search for various forms of dark matter in regions of particle physics parameter space complementary to underground and space-based searches to constrain the properties of dark matter [6].

### 3. Electrons

Above magnet spectrometers’ energy reach, where high energy trajectories are too straight to measure the particle momentum, ionization calorimetry, a high energy particle physics analog to the traditional measurement of heat energy with a calorimeter, has been used for cosmic ray particle energy determinations. In an ionization calorimeter, an incident particle’s energy is deposited inside an absorber via a cascade of nuclear and electromagnetic interactions. The energy of the primary particle is sub-divided among many secondary particles at each step of the cascade. Ultimately, the primary energy of an incident particle is dissipated via ionization and excitation of the absorbing material.

The most desirable material for an electron calorimeter would be one with a short radiation length ( $X_0$ ), while a hadron calorimeter should have a short interaction length ( $\lambda_I$ ) to force hadronic interactions near the top of the instrument, in addition to having sufficient material to absorb the cascades. Practical calorimeters for space applications are limited in absorber thickness, in order to have a reasonable cross-sectional area, i.e., geometrical factor for collecting the particles. The minimum depth depends on the energy resolution required for a particular experiment, but typically the electromagnetic shower should develop past its maximum within the calorimeter.

Another key factor for calorimetry is accurate charge measurement of the incoming particle. Albedo particles from the shower interactions can reach the charge detector and provide additional ionization signal, which can result in particle misidentification. Since the shower albedo increases with particle energy, the fraction of misidentified protons is likely to increase at higher energies [7]. Spatial segmentation in the charge detector combined with the tracking provided by the calorimeter can mitigate this problem. As shown in Fig. 3, the advanced thin ionization calorimeter (ATIC) was configured with an 18–22  $X_0$  deep, fully active bismuth germanate (BGO) calorimeter, preceded by a Silicon matrix for charge measurements. It incorporated a finely segmented (each pixel  $\sim 3 \text{ cm}^2$ ) charge detector to avoid the backscatter effect identified [8] as the cause of an apparent spectral bending reported by Grigorenko et al. [9] from their PROTON satellite measurements. The graphite target section ( $\sim 0.75 \lambda_{\text{int}}$ ) between the Silicon matrix

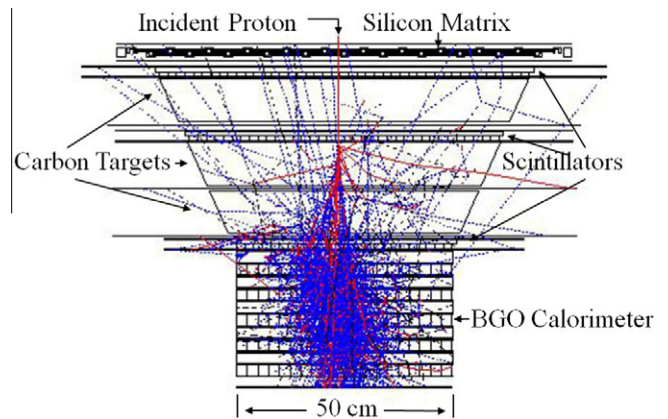


Fig. 3. A cross sectional view of the ATIC detector with an example of simulated proton shower.

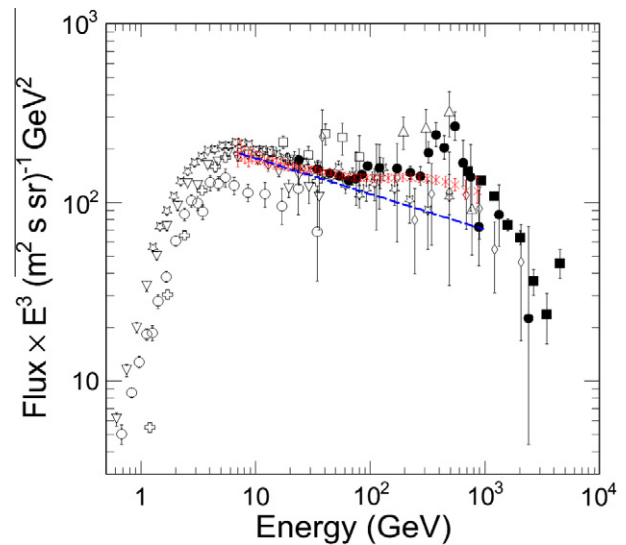


Fig. 4. The electron differential energy spectrum scaled by  $E^3$ : ATIC [10], filled circles; Fermi [11], red X; HESS [12], filled squares; PPB-BETS [13], upward open triangles; BETS [14], open squares; Sanriku [15], open diamonds; HEAT [16], downward open triangles; AMS-01 [17], open circles; CAPRICE [18], open crosses; PAMELA [19], open stars. (For interpretation of the references to colour in this figure legend, the reader is referred to the web version of this article.)

and the BGO calorimeter induces nuclear interactions of incident particles before they enter the calorimeter.

ATIC had three successful LDB flights from McMurdo, Antarctica, for a total of about 48 days above 99% of the Earth’s atmosphere: a 16-day flight from December 28, 2000 to January 13, 2001 (ATIC-1), a 20-day flight from December 29, 2002 to January 18, 2003 (ATIC-2), and a 20-day flight from December 26, 2007 to January 15, 2008 (ATIC-4). The third launch (ATIC-3) on December 18, 2005 suffered a balloon failure. The payload stopped ascending at an altitude of  $\sim 20$  km, and the flight was terminated about 4 h after the launch. ATIC-4 obtained only  $\sim 14$  days of science data due to loss of pressure in the gondola on January 11, 2008. The first two flights have generated interesting new results on the electron energy spectrum. The significant excess around  $\sim 600$  GeV [10] shown in Fig. 4, along with the positron to electron ratio,  $e^+/(e^- + e^+)$  enhancement [20] reported later by the Payload for anti-matter exploration and light-nuclei astrophysics (PAMELA), has generated considerable public and scientific interest due to speculation about their possible dark matter origin. The ATIC-4 instrument included a 25% thicker

calorimeter ( $22 X_0$ ). The additional calorimeter depth significantly improved the electron–proton separation and confirmed the ATIC-1 and -2 measurements [21].

Synchrotron radiation losses severely limit the flux of trans-TeV electrons from distant sources, which results in a spectral roll off. Nearby sources would appear as bumps and peaks, in addition to the distant source contribution. The source of the observed excess electrons would need to be a previously unidentified and relatively nearby cosmic object within about 1 kilo parsec (3260 light years) of the Sun. It could be an astrophysical source such as a pulsar, mini-quasar, supernova remnant, or even an intermediate mass black hole, but the ATIC data require rather unusual parameters for such objects [22].

Following the electron anomaly reported by ATIC, the Fermi gamma-ray space telescope (Fermi) collaboration [11] reported a less prominent excess over the same energy range, and the high energy stereoscopic system (HESS) collaboration [12] reported a steep electron spectrum roll off above 1 TeV. While these tantalizing signals from both space- and ground-based experiments could be interpreted as a signal of dark matter annihilation/decay, the difference between the ATIC and Fermi results around 600 GeV has been the subject of much debate. It should be noted Fermi was designed for gamma ray measurements up to 300 GeV. The ATIC and Fermi data are in a remarkably good agreement for a wide energy range ( $\sim 20$ –300 GeV), but the ATIC data show a more prominent peak than Fermi data above 300 GeV. The fact that the ATIC and Fermi data both begin to deviate from the conventional cosmic ray propagation model, i.e., continuation of the lower energy power law, (blue dashed line) at the same energy,  $\sim 100$  GeV, is important. The location of the maximum deviation is at  $\sim 600$  GeV for both measurements, although the amount of their excess (deviation) is about a factor of two higher for ATIC. The error bars for Fermi are smaller than for ATIC, due to its better statistics. However, ATIC is configured with a deeper calorimeter ( $18$ – $22 X_0$  vs.  $8.6 X_0$  for Fermi), so it has much better energy resolution (2% for ATIC versus  $\sim 20\%$  for Fermi). Fermi would be expected to see a smoother spectrum than ATIC due to the effect of this instrumental difference.

While these results might provide some information about the nature of dark matter, the resolution of their differences requires better understanding of the astrophysical and instrumental backgrounds. Improved results from current and upcoming direct and indirect searches will continue to shed light on these puzzles. A deep enough calorimeter for dedicated electron measurements in space may be required for a clearer picture. A new technique is being developed for a balloon-borne experiment to make ultrahigh energy (UHE) electron measurements. The cosmic ray electron-synchrotron telescope (CREST) will identify UHE electrons by observing the characteristic linear trail of synchrotron gamma rays generated as the electron passes through the Earth’s magnetic field [23]. A  $32 \times 32$  array of  $\text{BF}_2$  crystals individually viewed by photomultiplier tubes will result in effective detector area larger than the physical detector size (2.4 m on a side). CREST is expected to fly as an Antarctic LDB payload in the 2011–2012 season.

The electron excess, combined with the lack of antiproton excess in BESS [24], provides interesting constraints on dark matter models. The alpha magnet spectrometer (AMS) [17], which was launched to the International Space Station on May 16, 2011, has two orders of magnitude larger geometry factor than PAMELA. It will look for “smoking gun” signals from dark matter annihilation by measuring positrons, antiprotons, antideuterons,  $\gamma$ -rays and cosmic ray elements with great precision to the TeV energy scale. A major strength of AMS is that it can precisely measure all of these decay products simultaneously with a single instrument. It will undoubtedly be the leading experiment for indirect searches of dark matter this coming decade.

#### 4. Elemental spectra

Cosmic ray fluxes generally follow a power law that decrease rapidly as energy increases, presumably driven by cosmic shocks. Shock waves are observed to be the dominant particle acceleration process within the heliosphere, and they are believed to be prevalent in astrophysical plasmas on all scales throughout the universe. It is characteristic of diffusive shock acceleration that the resulting particle energy spectrum follows a power law for a wide range of parameters, or shock properties. This spectrum, when corrected for leakage from the Galaxy, should be consistent with the observed cosmic ray spectra. Although the properties of low energy data indicate that cosmic rays are accelerated in supernova shocks, details of acceleration mechanism and propagation of cosmic rays at high energies are not completely understood.

Elemental spectra of p, He, C, O, Ne, Mg, Si and Fe as a function of energy per particle are compared in Fig. 5. There is a general agreement among the existing data. The spectral roll off at low energies is due to the effect of solar modulation. For clarity, only AMS [17] and BESS [25] spectra are shown for the most abundant components, protons and helium: there are many magnet spectrometer data sets at low energies. Above 2 TeV, pioneering emulsion-based, passive calorimetry measurements were made by JACEE [29] and RUNJOB [30]. Both experiments were limited to

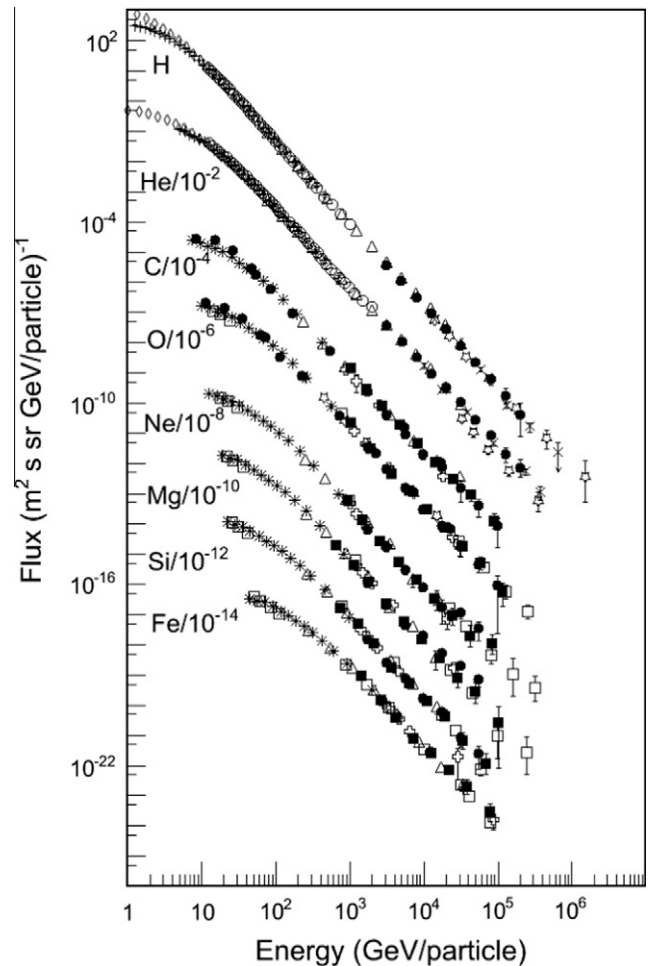


**Fig. 5.** Differential energy spectra from direct measurements of proton-to-Fe elements as a function of energy per particle. AMS [16], diamonds; BESS [24], crosses; ATIC-2 [25], open triangles; CREAM-1 [26], filled circles; CREAM-2 [27], filled squares; JACEE [28], x; RUNJOB [29], stars; HEAO-3 [30], asterisks; CRN [31], open crosses; TRACER [32], open squares.

charge group measurements using the emulsion and X-ray film techniques. These passive techniques limit the exposures because of the integrating effects of background [31]. Studies of long space-based exposures using these techniques would require frequent replacement of the emulsion plates and X-ray films.

Measurements of individual energy spectra of cosmic ray nuclei heavier than protons and helium at high energies have been performed with two missions in space: the high energy astrophysics observatory (HEAO-3) provided data with high statistical accuracy up to about 35 GeV/n [32]; and the cosmic ray nuclei (CRN) experiment on *Spacelab-2* performed the first measurements into the TeV/n region [33]. In addition, the balloon-borne transition radiation array for cosmic energetic radiation (TRACER) extended the heavy nuclei measurements to higher energies [34]. TRACER was configured with two layers of plastic scintillators ( $2\text{ m} \times 2\text{ m}$ ) for charge measurements, and a transition radiation detector to determine the Lorentz factor of the incident particle. A Cherenkov counter made of acrylic plastic at the bottom of the detector was used to reject non-relativistic particles. TRACER reported elemental spectra from oxygen ( $Z = 8$ ) to iron ( $Z = 26$ ) from a 14-day flight in Antarctica in 2003. Its second flight in 2006 from Sweden to Canada for 4.5 days extended its dynamic range to cover boron ( $Z = 5$ ) to iron ( $Z = 26$ ).

The ATIC data filled the gap between the low energy magnet spectrometer measurements and high energy emulsion-based data with individual charge resolution for elements from protons ( $Z = 1$ ) to iron ( $Z = 26$ ). There was an inconsistency between ATIC-1 [35] and ATIC-2 [26] data due to a trigger inefficiency. For high multiplicity (backscatter) events in which the six discriminators that feed an OR gate are all fired, the available current was insufficient for the OR to produce a trigger output, resulting in a missed trigger. Such high multiplicity of backscatter events occur as the incident particle energy increases and/or the charge of the nucleus increases. This leads to an energy dependent efficiency, reducing the number of events at high energy and steepening the energy deposited spectra. After the ATIC-4 flight, this effect was investigated in detail in the lab, which reproduced the behavior seen in flight [21]. The ATIC-2 data could be corrected due to a different hodoscope and trigger configuration, but ATIC-1 was not, leading to a reported spectrum for p and He that was steeper than it should have been. The effect of this trigger inefficiency is minimal for the electron observations, which are at lower energies with lower multiplicity.

As shown in Fig. 6 the CREAM instrument contains both a calorimeter and a TRD for energy measurements, and it has multiple charge detectors [36]. The highly segmented detectors comprising the instrument have about 10,000 electronic channels. The TRD and calorimeter, which can also measure the energy of protons and He, have different systematic biases in determining particle energy. The use of both instruments allows in-flight cross-calibration of the two techniques for  $Z > 3$  particles, which leads to a powerful method for measuring cosmic-ray energies [37]. In addition to the finely segmented silicon charge detector with  $2.12\text{ cm}^2$  pixels, CREAM utilizes both timing and Cherenkov techniques to minimize the effect of backscatter on charge measurements.

The CREAM calorimeter was designed to meet the challenging requirement to collect adequate statistics, yet stay within the weight limit for a balloon flight using a tungsten absorber and thin scintillating fibers. The radiation length for tungsten is 0.3 cm compared to 1.12 cm for BGO. Showers are sampled every radiation length in CREAM compared to the longitudinal segmentation of  $> 2 X_0$  in ATIC, giving more  $x, y$  measurements for the shower reconstruction. Energy deposition in the calorimeter determines the particle energy and provides tracking information to determine which segment(s) of the charge detectors to use for the charge measurement. Tracking for showers is accomplished by extrapolating each

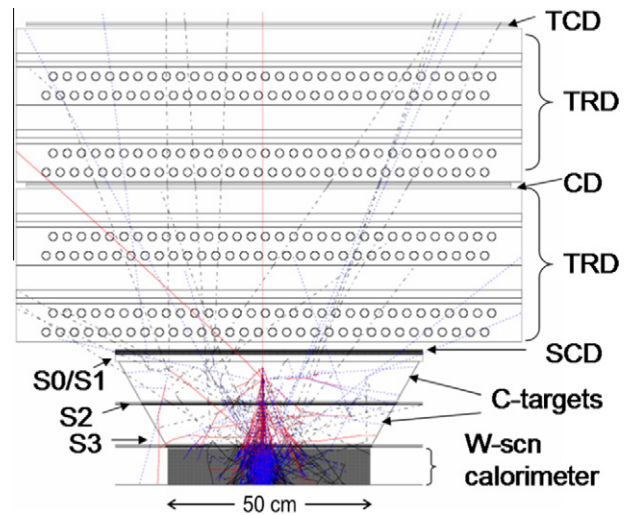


Fig. 6. A cross sectional view of the CREAM detector with an example of simulated proton shower.

shower axis back to the charge detectors. Tracking for non-interacting particles in the TRD is achieved with better accuracy (1 mm resolution with 67 cm lever arm, 0.0015 radians). The CREAM TRD provides a collection factor about 10 times that of ATIC for  $Z > 3$  nuclei.

Table 1 compares balloon-borne experiments for high energy measurements: CREAM [36], ATIC [38], TRACER [34], JACEE [29] and RUNJOB [30]. The energy measurement techniques are identified in Column 2, and the charge measurement ranges and charge resolutions are compared in Column 3. The CREAM TRD measures  $Z > 3$  particles with energy resolution of  $\sim 15\%$  for carbon and  $\sim 7\%$  for iron at a Lorentz factor  $\gamma = 3000$ . A TRD is suitable for the large area detectors for heavy nuclei and rare nuclear species, but its inherent response characteristics currently preclude measurements of p and He. The CREAM calorimeter measures all elements, including  $Z = 1$  and 2 particles, with energy resolution better than 45% for all energies.

As shown in Column 4, the CREAM flight duration exceeds the cumulative flight time of JACEE and RUNJOB. The CREAM payload is relatively light as an LDB payload (2000–2500 lb) compared to  $\sim 4100$  lb for BESS,  $\sim 3400$  lb for ATIC,  $\sim 3500$  lb for TRACER, etc. and it maintained high altitude. The corresponding atmospheric overburden was  $3.9\text{ g/cm}^2$ . That implies about  $6.8\text{ g/cm}^2$  for the maximum angle acceptance, which is smallest among the compared experiments. For example, the average vertical depth for RUNJOB was more than twice that of CREAM, due to its low flight altitude. Considering the RUNJOB acceptance of particles at large zenith angles, its effective atmospheric depth is as large as  $50\text{ g/cm}^2$ . For that depth, large corrections are required to account for the fact that 41% of protons and 84% of Fe nuclei would have interacted before reaching the detector.

The trigger geometry factor of the CREAM TRD is  $2.2\text{ m}^2\text{sr}$ . The effective geometry of the calorimeter, after taking into account the interaction fraction, is about  $0.3\text{ m}^2\text{sr}$  for protons and increasingly higher for heavier nuclei, due to their higher interaction probability. The collecting power of CREAM is about a factor of two larger than that of ATIC for protons and He. The effective exposures are compared in Column 6, and the observed numbers of high-energy protons are compared in Column 7. The number given for CREAM is our best estimate at the current stage of analysis, which is not yet complete. Nevertheless, the number of protons measured by CREAM far exceeds the total of all the prior experiments. JACEE reported only 656 protons above 6 TeV [29], despite the fact that the

**Table 1**

Comparison of balloon borne experiments for high-energy cosmic ray measurements.

Instrument	Energy measurement technique	Charge range and resolution	Flight duration	Atmospheric depth <sup>a</sup> (g/cm <sup>2</sup> )	Effective exposure (m <sup>2</sup> -sr-days)	Observed number of protons >6 TeV
ATIC	Calorimeter (0.75 $\lambda_i$ , 18 $X_0$ )	$1 \leq Z \leq 28$ $\Delta Z = 0.3$	~48 days	4.3 (7.9)	5	~720
TRACER <sup>a</sup>	TRD	$8 \leq Z \leq 28$ $\Delta Z = 0.3$ (O) 0.5 (Fe)	~10 days	3.9 (9.2)	50	None
		$3 < Z \leq 28$ $\Delta Z = 0.3$ (O) 0.5 (Fe)	~4 days		20	
CREAM	Calorimeter (0.5 $\lambda_i$ , 20 $X_0$ )	$1 \leq Z \leq 28$ $\Delta Z = 0.2$	~160 days	3.9 (6.8)	48	>5000
	TRD	$3 < Z \leq 28$ $\Delta Z = 0.2$	~42 days	3.9(7.9)	55	None
JACEE	Emulsion (~0.05 $\lambda_i$ , ~4 $X_0$ )	$1 \leq Z \leq 28$ Charge group	~60 days (1436 m <sup>2</sup> hr)	5.3 (28)	~10 (644 m <sup>2</sup> hr)	656
RUNJOB	Emulsion (~0.2 $\lambda_i$ , ~4 $X_0$ )	$1 \leq Z \leq 28$ Charge group	~60 days (575 m <sup>2</sup> hr)	10 (48)	6 (p); 24 (>C)	Close to JACEE

<sup>a</sup> The average vertical depth is shown with the maximum depth considering the angle acceptance in parentheses.

flight duration was about 60 days. This is, in part, because less than half of their collected data was analyzed and, in part, because their detection efficiency was apparently low. RUNJOB had about the same flight duration, but only 40% of the exposure due to smaller detector area. TRACER has a larger geometry factor than CREAM, but a smaller dynamic range for charge measurements ( $Z = 8$ –26 and  $Z = 3$ –26, respectively, for its two flights).

The elemental spectra are shown as a function of energy per nucleon in Fig. 7. Here the observed fluxes are multiplied by  $E^{2.75}$ , to facilitate high energy spectral comparison. An extrapolation of the magnet spectrometer spectra, e.g., BESS [25] spectra with indices of  $2.732 \pm 0.011$  for protons from 30 GeV to a few hundred GeV, and  $2.699 \pm 0.040$  for helium from 20 GeV/n to a few hundred GeV/n would appear as nearly horizontal lines. Overall, recent CREAM data are consistent with previous measurements, namely JACEE [29] and ATIC-2 [26] for protons and helium and HEAO-3 [32], CRN [33] and TRACER [39] for heavy nuclei where they overlap. The RUNJOB data for helium fluxes are much lower than the data of CREAM, ATIC-2 and JACEE. This also holds true for other groups of nuclei.

The compiled data in Fig. 7 show similar spectral shapes with a broad plateau around 20–200 GeV/nucleon for each element. They also show a harder spectrum for each element above ~200 GeV/nucleon, indicating departure from a single power law. CREAM reported a broken power law fit to C–Fe data with an index  $\gamma_1 = -2.77 \pm 0.03$  below 200 GeV/n and  $\gamma_2 = -2.56 \pm 0.04$  above 200 GeV/n [40]. The spectral index  $\gamma_1$  is consistent with the low energy helium measurements, e.g., AMS [17], BESS [25], and PAMELA [41], whereas  $\gamma_2$  agrees remarkably well with the CREAM helium index of  $-2.58 \pm 0.02$  at higher energies. A single-power law fit to the CREAM data [28] gives a spectral index of  $-2.66 \pm 0.04$ , which agrees with the TRACER O – Fe power-law fit index of  $2.67 \pm 0.08$  [39]. Note that there is only one TRACER data point between ~10 GeV/nucleon and ~400 GeV/nucleon, where the spectral shape changes. JACEE and RUNJOB did not report spectra of individual elements heavier than helium. The pervasive discrepant hardening in all of the observed elemental spectra contradict the traditional view that a simple power law can represent cosmic rays without deviations below the “knee” around  $3 \times 10^{15}$  eV, and it provides important constraints on cosmic ray acceleration and propagation models.

Whether or not the proton spectrum index is the same as that of heavier nuclei has long been a tantalizing question. JACEE [29] reported a difference in the spectral indices for p and He, but RUNJOB [30] did not see such a difference. More recently, CREAM reported that proton and helium spectra are not the same, and the helium spectrum is harder than the proton spectrum. The reported indices are  $-2.66 \pm 0.02$  for protons and  $-2.58 \pm 0.02$  for helium, respectively [42]. CREAM measurements at high energies, where no solar

modulation effect is expected, show this difference clearly over a wide energy range. The CREAM proton and helium fluxes are somewhat lower than the fluxes reported by ATIC-2, but both CREAM and ATIC-2 measurements show harder spectra than the lower energy measurements (e.g. [17,25]). Data from ATIC with its (much-deeper-than-JACEE) fully-active calorimeter, which contains the electromagnetic shower maximum, are in better agreement with the space-based and balloon-borne magnet spectrometer data than old calorimeter measurements [43] at lower energies.

It has been difficult to prove the subtle difference between proton and helium spectra, because spectral indices determined from measurements over the limited energy range of a single experiment could not provide a definitive answer. For most magnet spectrometers, the energy range for a power law fit was less than ~a decade due to solar modulation effect at low energies. Although the residual solar modulation effect is expected to be small above ~10 GV, depending on the time of measurements, a slightly different low energy end point of the power law fit could result in a different spectral index. Note, also, that experiment-to-experiment index variations for the low energy data are larger than their quoted fit errors, probably due to different energy ranges for their fits and residual effects of solar modulation.

As shown in Fig. 8, the proton-to-helium ratio of  $8.9 \pm 0.3$  at ~9 TeV/nucleon reported by CREAM [42] is significantly lower than the lower energy measurements, i.e.,  $18.8 \pm 0.5$  by AMS at 100 GeV/nucleon, ~18 by CAPRICE and ~16 by BESS. The CREAM result agrees with the JACEE H/He ratio, ~12.5 at ~10 TeV. The ATIC data show a ratio close to the magnet spectrometer measurements at low energies, and clear changes as a function of energy.

Although the observed index difference appears small, Ohira and Ioka [44] have pointed out that enhancement of helium relative to protons is amazing, because the mean helium abundance in the universe is virtually constant. Big Bang nucleosynthesis is indispensable for explaining the cosmic helium abundance, since stellar nucleosynthesis does not enhance the mean helium abundance. Ohira and Ioka proposed a chemically enriched region, such as a superbubble, to explain the different spectra. If the difference is the effects of spallation, as suggested by Blasi and Amato [45], it would mean that the Galactic diffusion is characterized by a low value of  $\delta$  (1/3 compared to 0.6), where the diffusion coefficient  $D(E) \propto E^\delta$ .

The PAMELA space mission uses a permanent magnet spectrometer with a variety of detectors for precision measurements of the abundance and energy spectra of cosmic rays. The energy reach of the high quality PAMELA data is very limited, but it measures electrons, positrons, antiprotons, and light nuclei over the energy range from 50 MeV to hundreds of GeV, depending on the species. PAMELA [41] has recently reported direct observation of hardening of proton and Helium spectra around 200 GV, similar to the spectral

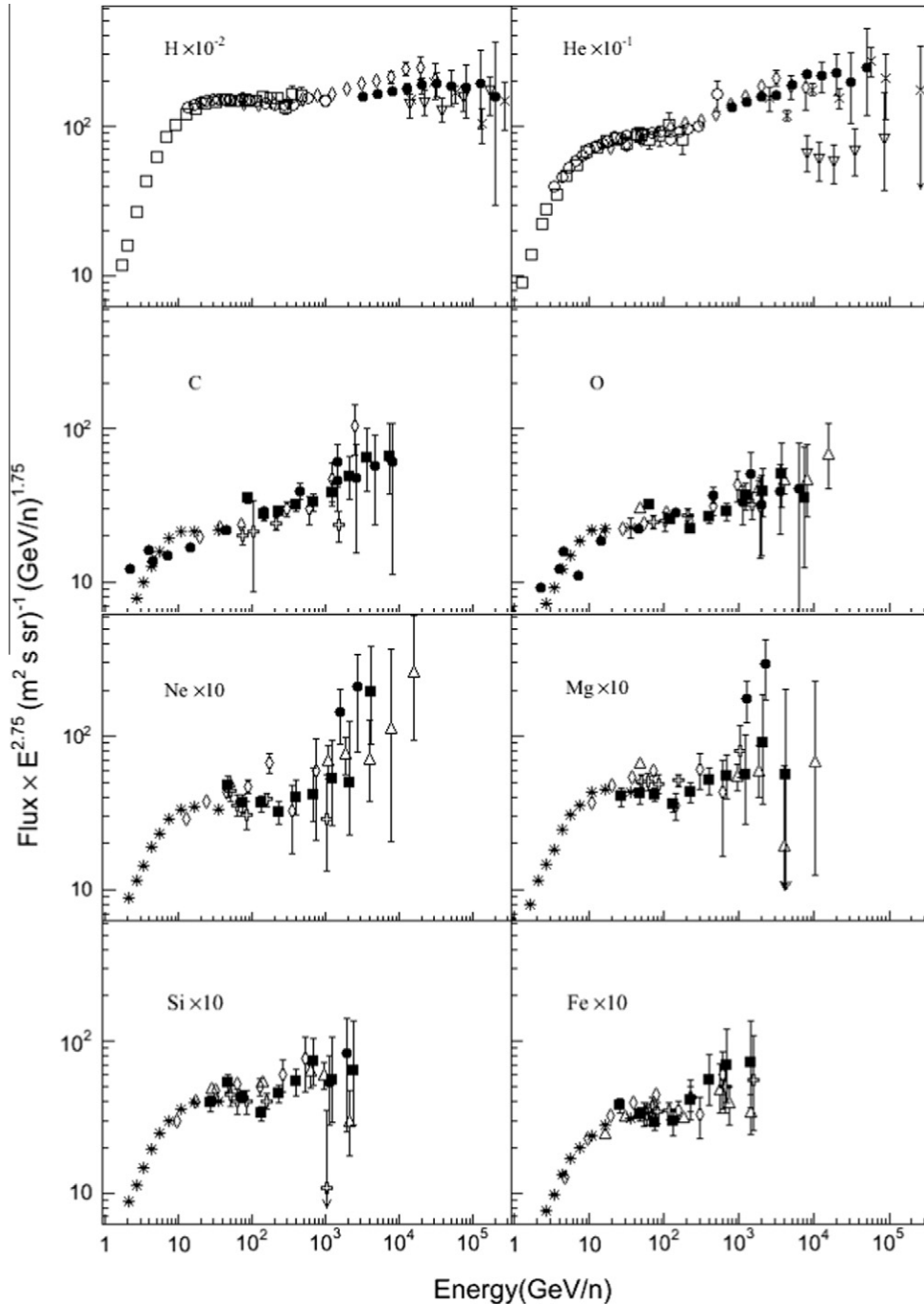


**Fig. 7.** The energy spectra of elements from protons to Fe as a function of energy per nucleon (scale by  $E^{2.75}$ ). BESS (open squares), PAMELA (open circles), ATIC-2 (open diamonds), CREAM-1 (filled circles), CREAM-2 (filled squares), HEAO-3 (asterisks), TRACER (open triangles), JACEE (X), and RUNJOB (open inverted triangles). Some of the overlapping BESS and PAMELA data points are not shown to achieve better clarity.

hardening first reported by CREAM [40]. The experimental data are not precise enough to debate the exact starting point of the hardening, whether it is 200 GV or 200 GeV/n. The coincidence that the observed spectral flattening of each element, including protons, at an energy similar to the electron enhancement indicates that a single mechanism might be responsible for all the elements, as well as electrons, which could imply the existence of hadron sources within distances comparable to the range of electrons travelling through the interstellar medium. Although a one-to-one correlation cannot be made, the observed flattening might be related to the 10 TeV anisotropy reported recently by the Milagro collaboration, if it is due to a cosmic-ray accelerator [46].

In earlier days, a bend or roll-off in the proton spectrum was reported to occur near 2 TeV [9], which was likely due to the effect of backscatter effect on the charge measurements [8]. JACEE and ATIC data indicated a bend around 40 TeV and 20 TeV, respectively, although the JACEE collaboration decided their statistics was too low for any conclusive evidence. These roll-off energies for protons are about an order of magnitude below the expected cut-off for supernova remnant shock acceleration and  $\sim 2$  orders of magnitude below the “knee” [48] seen in the all-particle spectrum. Limited statistics may have precluded assertions that the helium spectrum steepens, as the proton spectrum appeared to do. All the plots show only statistical uncertainties, and there are additional

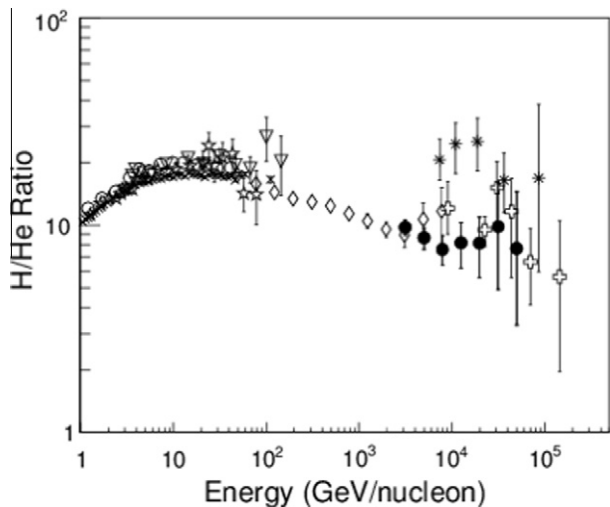


**Fig. 8.** Proton to Helium ratio as a function of energy per nucleon: CREAM-I, filled circles; ATIC, diamonds; CAPRICE-94, stars; CAPRICE-98, downward open triangles; LEAP [47], open circles; JACEE, open crosses; RUNJOB, asterisks; PAMELA, x.

systematic errors not shown. There are insufficient statistics for detection of spectral features above  $\sim 20$  TeV for even the most dominant components, H and He. The detailed energy dependence of the elemental spectra, measured to the highest energy possible, holds the “key” to understanding the acceleration (and galactic propagation) for the bulk of cosmic rays, i.e., those at energies below the knee in the all-particle spectrum.

## 5. Propagation history

The spectra of cosmic rays measured at Earth are different from their source spectra, and understanding this difference is crucial for solving the puzzle of cosmic-ray origin. Secondary nuclei are particularly useful in addressing this goal, because they are produced largely by spallation of primary particles as they propagate from their source regions through the interstellar medium to Earth. Earlier measurements have shown that the diffusion escape time for particles from our Galaxy decreases with increasing particle energy, or magnetic rigidity. The escape time can be characterized as a pathlength (in  $\text{g}/\text{cm}^2$ ). A typical form for the rigidity dependence of this quantity is  $\lambda = \lambda_0(R/R_0)^{-\delta}$ , where  $\lambda$  is the mean escape pathlength,  $R$  is the nucleus magnetic rigidity, and  $\delta$  is an energy dependent parameter. The simplest propagation model is one in which the Galaxy is pictured as a large containment volume with a small probability for particles to escape at the boundary—the so-called standard leaky-box model (SLBM) (e.g. 51). Propagation in this model is described by the mean of the path length distribution.

The measured B/C ratios are compared with propagation models in Fig. 9. The CREAM data are consistent with the HEAO-3 experiment at low energies, and ATIC and TRACER where they overlap. The curves represent three different  $\delta$  values for the SLBM, as well as a reacceleration model [52]. The data indicate that the propagation pathlength of cosmic ray nuclei is smaller by an order of magnitude for particles in the TeV/n region compared to those at energies below 10 GeV/n. This high-energy path length ( $\sim 1 \text{ g}/\text{cm}^2$ ) is still large compared to the typical grammage of the Galactic disk ( $\leq 0.002 \text{ g}/\text{cm}^2$ ), so it does not significantly constrain residual pathlength models proposed for higher energies [53], in the source region [54], or by a reacceleration model [52].

Balloon borne experiments have provided the highest energy B/C data and other relative abundances (e.g. 55). The uncertainty in the contribution of atmospheric boron becomes significant above  $\sim 100$  GeV/n, where the contribution from charge-changing

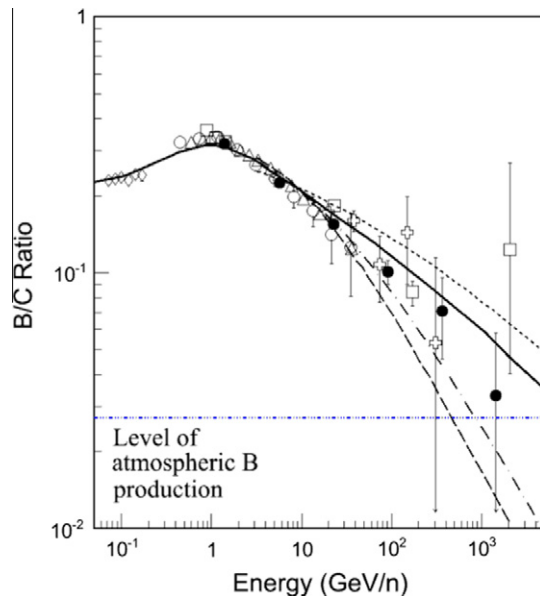


**Fig. 9.** B/C ratio data: CREAM-I, black circles; ATIC, open crosses; HEAO-3, open triangles; TRACER [49], open squares, AMS-01, open circles; and ACE [50], open diamonds. The curves represent power law mean pathlength with  $\delta = 0.333$ , dotted line;  $\delta = 0.6$ , dash-dot line; and  $\delta = 0.7$ , dashed line, for SLBM; and a solid line for a reacceleration model. A horizontal blue dash-dot line represents the level of atmospheric boron production. (For interpretation of the references to colour in this figure legend, the reader is referred to the web version of this article.)

interactions in the atmosphere is similar in amount to the total production of boron during propagation through the Galaxy. Consequently, accurate measurements of B/C on high-altitude balloon experiments are limited by systematic errors in the TeV/n region. To unravel the acceleration and propagation enigma, the next experimental step lies in composition measurements, which not only extend the range of energies and improve statistics, but also include the secondary nuclei below  $Z = 26$ . Such measurements require very large exposure factors, excellent charge resolution, and identification of atmospheric background for balloon-borne investigations.

## 6. Source abundances

When comparing the galactic cosmic ray (GCR) source (GCRS) abundances with solar system (SS) abundances as a function of the first ionization potential (FIP), there is a general trend of lower GCR/SS with higher FIP [56]. Likewise, the same GCRS/SS ratios, as a function of elemental atomic mass, show a separation of refractory elements and volatile elements. The GCRS/SS ratio is generally higher for refractory elements than for volatile elements, as illustrated in Fig. 10.

The trans-iron galactic element recorder (TIGER) had two balloon flights over Antarctica totaling 50 days at float. The first launch was on December 21 2001, and the second launch was on December 17, 2003: they had 32-day and 18-day flights, respectively. Using two Cherenkov counters with Aerogel and acrylic radiators and a pair of scintillating fiber hodoscopes sandwiched between two scintillators, TIGER measured the elemental composition of the rare GCR heavier than iron, looking for clues to nucleosynthesis and the origin of cosmic rays. TIGER obtained the best measurement to date of abundances of  $^{31}\text{Ga}$ ,  $^{32}\text{Ge}$ , and  $^{34}\text{Se}$ . Rauch et al. [57] reported that the data are best organized when the GCRS abundances are compared with SS including 20% massive star outflow (MSO), and they follow two different power-law trends:  $A^{2/3}$  for the refractory elements and  $A^1$  for volatile elements. As shown in Fig. 10, CREAM TeV data are in agreement with TIGER/HEAO-3 at

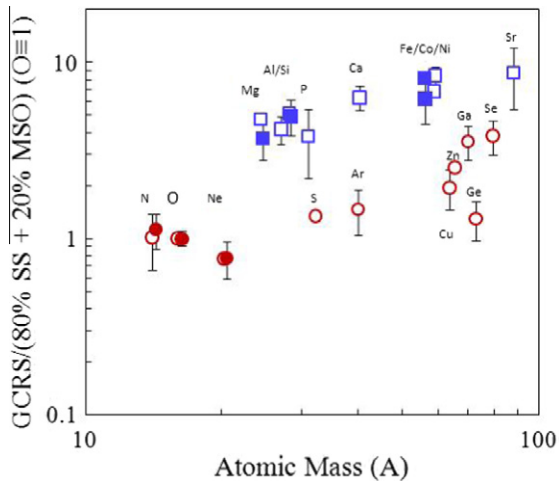


**Fig. 10.** Ratio of cosmic-ray source abundances to a mixture of 80% SS and 20% MSO as a function of atomic mass. CREAM data [55] (filled symbols) in the energy range from 500 GeV/n to  $\sim 4$  TeV/n are compared to those of HEAO and TIGER data [57] (open symbols) below 30 GeV/n. Refractory elements (blue squares) and volatile elements (red circles). (For interpretation of the references to colour in this figure legend, the reader is referred to the web version of this article.)

lower energies. The data are consistent with the idea of GCR origin in OB associations [58], i.e., cosmic rays come from the core of super-bubbles, where OB associations enrich the interstellar medium with the outflow of massive stars (Wolf–Rayet phase and Supernovae) [59]. The data also imply preferential acceleration of elements found in interstellar grains [60,61] compared with those found in interstellar gas, as well as mass-dependent acceleration.

A larger version of TIGER, Super-TIGER,  $5 \text{ m}^2$  compared to  $\sim 1 \text{ m}^2$  for TIGER, is being developed to measure the elements in the interval  $30 < Z < 42$  with individual element resolution and high statistical precision, and to make exploratory measurements through  $Z = 60$  [62]. The first LDB flight is planned for launch in December 2012.

## 7. Relevance to ultrahigh energy cosmic rays

Recent paradigm-breaking observations show the need for a renewed focus on high statistics studies of cosmic rays at high energies, which are key to understanding details of the supernova shock acceleration process. As shown in Fig. 11, the all-particle spectrum obtained by summing up CREAM elemental spectra is consistent with previous measurements. Uncertainties in the current intriguing results are still large, and they can be reduced only with better statistics. At the ultrahigh energy end, ground-based indirect measurements from  $\sim 10^{15}$  eV to  $\sim 10^{20}$  eV have established the existence of the “knee” [48], as well as the “ankle” related to the Greisen–Zatsepin–Kuzman (GZK) cutoff around  $5 \times 10^{19}$  eV [63,64]. Ground-based observations of air showers have the great advantage of large collecting power, but interpretation of the observations depend on hadronic interactions of cosmic rays with air nuclei and the production of secondary particles at energies above the available collider energies. Modern air shower arrays employ complementary techniques, such as arrays of scintillators, air Cherenkov detectors, etc. to measure simultaneously as many air-shower parameters as possible, in order to reduce the model dependence in energy reconstruction. Some composition-sensitive shower observables (e.g., shower maximum location) are analyzed in an attempt to infer the mean primary mass as a function of energy near the knee region (e.g., 65,66). Future CREAM flights will extend the energy reach of direct measurements to higher energies to distinguish hadronic interaction models such as QGSJET [67] and SIBYLL [68], used for interpreting ground-based indirect measurements.

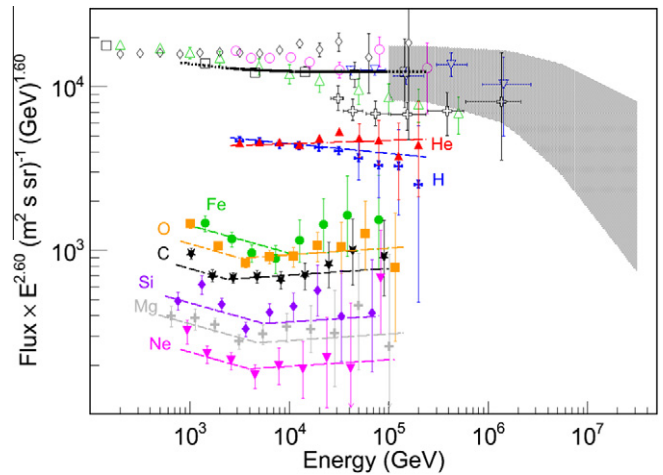


**Fig. 11.** The all-particle spectrum (black solid curve) obtained by summing up CREAM elemental spectra from p to Fe (filled symbols) is compared with previous measurements (open symbols): ATIC-1 [35], black squares; JACEE, blue downward triangles; RUNJOB, black crosses; Ichimura et al. [71], green upward triangles; SOKOL [72], pink circles. The gray shaded area indicates ground based indirect measurements. (For interpretation of the references to colour in this figure legend, the reader is referred to the web version of this article.)

CREAM has accumulated an exposure of  $\sim 160$  days in six Antarctic long-duration balloon (LDB) flights while waiting for the ultra long duration balloon (ULDB) vehicle to become operational. This is currently the primary supply of TeV scale cosmic ray data.

The balloon-borne antarctic impulsive transient antenna (ANITA) was designed to probe ultra high energy neutrinos. ANITA searches for impulsive coherent radio Cherenkov emission in the 200–1200 MHz range from the Askaryan effect. Neutrinos can reach the Earth without being attenuated, and they are of particular interest at the GZK cutoff, where other particles and photons would interact with the cosmic microwave background and be unable to propagate over long distances. ANITA has flown twice in Antarctica in 2006 and 2008. Their constraint on cosmogenic neutrino models excludes several mainstream models with very flat source energy spectra [69]. ANITA-1 also reported observation of 16 ultra high energy cosmic ray events via radio pulses originating from interactions of the cosmic ray air shower with the geomagnetic field, a process known as geosynchrotron emission [70]. Their plan is to improve sensitivity by a factor of 3 with a better hardware trigger and more antennas for ANITA-3, which will be optimized for both ultra high energy cosmic rays and neutrinos, and they expect to detect  $\sim 350$ –500 cosmic ray events.

## 8. Discussions and Conclusions

It has been almost one hundred years since Hess' discovery of cosmic rays, energetic particles from space. There have been many advances in recent years in both the measurements of cosmic rays and in the models describing their acceleration and propagation through the Galaxy. Yet, the exact origin of these ubiquitous particles remains elusive. Cosmic rays, as observed in satellite, balloon, and ground-based detectors, cover enormous energy and elemental ranges. Ground-based measurements have shown that cosmic ray energies could be as high as  $10^{20}$  eV, far exceeding the reach of any man-made accelerators. Space-based experiments have the advantage of direct measurements of cosmic rays before they breakup in the atmosphere. Recent advances in understanding TeV cosmic rays through new data and theoretical models, along with prospects for future measurements, have been discussed in this paper. In summary, (1) Proton and Helium spectra are different, (2) Hi-Z spectra are consistent with Helium, (3) elemental

spectra are not pure power laws but show hardening above  $\sim 200$  GeV/n, and (4) there is an excess electrons ( $e^- + e^+$ ) at high energies.

The electron anomaly [10,11,20] has triggered a lot of interpretation attempts, due to its possibility as a signal of dark matter. The feature is probably too low in energy and too narrow in energy to be the signature for a standard SNR source of GCR electrons. Microquasars probably can not generate electrons with energy much above  $\sim 10$  GeV. A pulsar could be the source but it would need to be unusually efficient in generating  $e^+e^-$  pairs, and it would need to have a very steep energy spectrum [22].

Annihilation of an exotic dark matter particle could explain the observed excess electrons and the WMAP microwave “haze”, but new physics is needed to do this. It is hard to accommodate within the minimal supersymmetric standard model (MSSM). Considering the anti-proton and gamma-ray constraints, the data prefer models with mostly leptonic annihilation channels (muons), i.e., leptophilic (e.g. 73). Most models predict rather large masses ( $>1$  TeV), and need an additional “boosting factor” that could be achieved with enhanced cross sections or clumpy distribution of dark matter. Most models also make testable predictions, such as gamma-ray enhancement, which should be observable with Fermi and AMS.

The origin of excess electrons, whether it is an astrophysical source or an exotic source, cannot be understood based on the lepton data alone. The key is to look at the lepton spectrum in conjunction with data for other cosmic-ray species and cosmic-ray propagation models. Understanding the cosmic-ray background is key to the interpretation of these data, and extending the measurements to higher energies is particularly important. The current cosmic-ray propagation and acceleration models are based on the existing low energy data, and their extension to high energy cannot be validated until high-energy measurements are made.

The current data indicate that the origin of cosmic rays is more complex than previously expected. An explanation for the difference between proton and helium spectra could be that they are coming from different types of sources or acceleration sites. For example, protons might come mainly from the supernova explosion of a low mass star directly into the interstellar medium. Helium and heavier nuclei might come mainly from the explosion of a massive star into the atmosphere swept out by the progenitor star rather than directly into the general interstellar medium [74,75].

The spectral hardening above  $\sim 200$  GeV/n could imply that the source spectra are harder than previously thought, based on the low energy data, or the hardening could reflect the predicted concavity in the spectra before the “knee” [76]. In the framework of diffusive shock acceleration cosmic-ray pressure created by particle interactions with the shock could broaden the shock transition region, causing higher energy particles to gain energy faster. This could result in spectral flattening with increasing cosmic-ray energy and deviations from a pure power law [77]. The observable effect is expected to be small when summed over multiple sources and propagated over Galactic distances [78], but the possible observation of concavity would provide evidence that cosmic rays are dynamically important in the acceleration process.

Alternatively, the observed spectral hardening could be due to nearby sources, as suggested for the recent electron observations [10–12]. The substantial contribution of a nearby and recent single source (supernova remnant or pulsar) to the flux of protons and nuclei has been proposed [79] to explain the “knee”. A multi-source model by Zatsepin and Sokolskaya [80] considered novae stars and explosions in superbubbles as additional cosmic-ray sources. Whether it results from a nearby isolated supernova remnant [81] or the effect of distributed acceleration by multiple remnants embedded in a turbulent stellar association [82] is another question.

Whatever the explanation, spectral hardening must be accounted for in explanations of the electron anomaly and cosmic ray “knee”. Donato and Serpico [83] reported that the spectral hardening reported by CREAM would lead to appreciable modifications for the secondary yields, such as antiprotons and diffuse gamma rays, in the sub-TeV range. They concluded that using a simple power law to model the astrophysical background for indirect dark matter searches, as often done in the literature, might lead to wrong conclusions about the evidence of a signal. Or, if a signal should be detected, use of a power law could lead to bias in the inferred values of the parameters describing the new phenomena. Since high energy stable nuclei have long range propagation (e.g. [84]), it is likely that this spectral inflection is not merely local but pertains to a few kpc scale around the Earth [85]. Therefore, a consistent prediction of the secondary positron flux should take it into account.

Ballooning offers cutting-edge science discoveries with state-of-the-art instruments in a rapid turn-around environment. Driven by science, these investigations also play important roles in training of experimental space scientists and engineers, and in development of new instruments for future spaceflight. The attainment of month-long flight duration in two and three circumnavigations of Antarctica made it possible to collect unprecedented data. NASA is currently developing a super-pressure balloon (SPB) capable of maintaining high-altitude, ULDB flights at any latitude with loads comparable to zero-pressure balloons [1]. SPB's are essentially constant volume systems that require the balloon skin (gas bag) to be strong enough to withstand the pressurization caused by solar radiation heating of the gas during the day, and still remain pressurized at night after the gas has cooled. The current SPB concept has a lobed structural design, which has a pumpkin-like shape that allows clear separation of the load-transferring functions of the major structural elements of the pneumatic envelope, the tendons and the film. No ballast is required to maintain altitude as long as the balloon remains fully inflated, i.e., pressurized. A 0.2 MCM SPB flew successfully for 54 days in Antarctica between December 2008 and February 2009, and a 0.4 MCM SPB completed its successful 22-day flight in January 2011. A 0.5 MCM SPB test flight is planned for launch during the 2011–2012 Antarctic season. The 0.74 MCM balloon is approximately the size still intended for the ULDB demonstration mission of 60–100 days with a 1000 kg science instrument.

As ULDB becomes available, long-duration exposures can be achieved faster and more efficiently without multiple refurbishment and launch efforts. Whatever the flight duration (either LDB or ULDB), the data from each flight reduces the statistical uncertainties and extends the reach of measurements to energies higher than previously possible. New and continuing experiments are expected to provide further information over the next several years.

## Acknowledgments

The author thanks the NASA Wallops Flight Facility Balloon Program Office, the Columbia Scientific Balloon Facility, the National Science Foundation Office of Polar Programs, and Raytheon Polar Services Company for the successful balloon launches, flight operations, and payload recoveries. This work was supported by NASA grants NNX08AC52G, NNX10AC47G, and their predecessor grants.

## References

- [1] W.V. Jones, Evolution of scientific research ballooning, in: Proceedings 29th International Cosmic Ray Conference, Pune, vol. 10, 2005, pp. 173–184.
- [2] E.S. Seo et al., CREAM collaboration, CREAM: 70 days of flight from 2 launches in Antarctica, *Adv. Space Res.* 42 (2008) 1656–1663.
- [3] A.W. Strong, I.V. Moskalenko, V.S. Ptuskin, Cosmic-ray propagation and interactions in the Galaxy, *Annu. Rev. Nucl. Part. Sci.* 57 (2007) 285–327.

- [4] K. Abe et al., Search for Antihelium with the BESS-Polar Spectrometer, *Phys. Rev. Lett.* 108 (2012) 131301.
- [5] H. Fuke et al., Search for cosmic-ray antideuterons, *Phys. Rev. Lett.* 95 (2005) 081101.
- [6] C.J. Hailey et al., An indirect search for dark matter using antideuterons: the GAPS experiment, *New J. Phys.* 11 (2009) 105022.
- [7] E.S. Seo et al., The advanced thin ionization calorimeter (ATIC) experiment: expected performance, in: *Proceedings of SPIE International Symposium on Optical Science, Engineering, and Instrumentation*, vol. 2806, 1996, pp. 134–144.
- [8] R.W. Ellsworth et al., On the high energy proton spectrum measurements, *Astrophys. Space Sci.* 52 (1977) 415–427.
- [9] N.L. Grigorov et al., Energy spectrum of primary cosmic rays in the  $10^{11}$  to  $10^{15}$  eV energy range according to the data of Proton-4 Measurements, in: *Proceedings 12th International Cosmic Ray Conference*, vol. 5, 1971, pp. 1746–1751.
- [10] J. Chang et al., An excess of cosmic ray electrons at energies of 300–800 GeV, *Nature* 456 (2008) 362–365.
- [11] A.A. Abdo et al., Measurement of the cosmic ray  $e^+ + e^-$  spectrum from 20 GeV to 1 TeV with the Fermi large area telescope, *Phys. Rev. Lett.* 102 (2009) 181101.
- [12] F. Aharonian et al., Energy spectrum of cosmic-ray electrons at TeV energies, *Phys. Rev. Lett.* 101 (2008) 261104.
- [13] S. Torii et al., High-energy electron observations by PPB-BETS flight in Antarctica, 2008 arXiv:0809.0760v1.
- [14] S. Torii et al., The energy spectrum of cosmic-ray electrons from 10 to 100 GeV observed with a highly granulated imaging calorimeter, *Astrophys. J.* 559 (2001) 973–984.
- [15] T. Kobayashi et al., High energy cosmic-ray electrons beyond 100 GeV, in: *Proceedings 26th International Cosmic Ray Conference*, vol. 3, 1999, pp. 61–64.
- [16] M.A. DuVernois et al., Cosmic-ray electrons and positrons from 1 to 100 GeV: measurements with heat and their interpretation, *Astrophys. J.* 559 (2001) 296–303.
- [17] M. Aguilar et al., the AMS collaboration, The alpha magnetic spectrometer (AMS) on the international space station. Part I. Results from the test flight on the space shuttle, *Phys. Rep.* 366 (2002) 331–404.
- [18] M. Boezio et al., The cosmic-ray electron and positron spectra measured at 1 AU during solar minimum activity, *Astrophys. J.* 532 (2000) 653–669.
- [19] O. Adriani et al., Cosmic-ray electron flux measured by the PAMELA experiment between 1 and 625 GeV, *Phys. Rev. Lett.* 106 (2011) 201101.
- [20] O. Adriani et al., An anomalous positron abundance in cosmic rays with energies 1.5–100 GeV, *Nature* 458 (2009) 607–609.
- [21] J.P. Wefel et al., The spectra of cosmic rays from the three flights of ATIC, in: *Presentation at the 38th COSPAR scientific Assembly*, Bremen, 2010.
- [22] S. Profumo, Dissecting cosmic-ray electron-positron data with Occam's Razor: the role of known Pulsars, 2008, <arXiv:0812.4457[astro-ph]>.
- [23] S. Nutter et al., The cosmic ray electron synchrotron telescope (CREST), in: *Proceedings 31st International Cosmic Ray Conference*, 2009, p. 1412.
- [24] K. Abe et al., Measurement of cosmic-ray low-energy antiproton spectrum with the first BESS-polar antarctic flight, *Phys. Lett. B* 670 (2008) 103–108.
- [25] S. Haino et al., Measurements of primary and atmospheric cosmic-ray spectra with the BESS TeV spectrometer, *Phys. Lett. B* 594 (2004) 35–46.
- [26] D. Panov et al., Energy spectra of abundant nuclei of primary cosmic rays from the data of ATIC-2 experiment: final results, *Bull. Russian Acad. Sci. Phys.* 73 (2009) 564–567.
- [27] H.S. Ahn et al., the CREAM collaboration, Measurements of cosmic ray secondary nuclei at high energy by the first flight of the CREAM balloon experiment, *Astropart. Phys.* 30 (2008) 133–141.
- [28] H.S. Ahn et al., the CREAM collaboration, Energy spectra of cosmic ray nuclei at high energies, *Astrophys. J.* 707 (2009) 593–603.
- [29] K. Asakimori et al., Cosmic-ray proton and helium spectra: results from the JACEE experiment, *Astrophys. J.* 502 (1998) 278–283.
- [30] V.A. Derbina et al., Cosmic-ray spectra and composition in the energy range of 1.0–1000 TeV per particle obtained by the RUNJOB experiment, *Astrophys. J.* 628 (2005) L41–L44.
- [31] V. Kopenkin, T. Sinzi, Cosmic ray primary composition in the energy range 10–1000 TeV obtained by passive balloon borne detector: reanalysis of the RUNJOB experiment, *Phys. Rev. D* 79 (2009) 072011.
- [32] J.J. Engelmann et al., Charge composition and energy spectra of cosmic ray nuclei for elements from Be to Ni – results from HEAO-3-C2, *Astron. Astrophys.* 233 (1990) 96–111.
- [33] D. Müller et al., Energy spectra and composition of primary cosmic rays, *Astrophys. J.* 374 (1991) 356–365.
- [34] M. Ave et al., Composition of primary cosmic-ray nuclei at high energies, *Astrophys. J.* 678 (2008) 262–273.
- [35] H.S. Ahn et al., The energy spectra of proton and helium measured with the ATIC experiment, *Adv. Space Res.* 37 (2006) 1950–1954.
- [36] H.S. Ahn et al., the CREAM collaboration, The cosmic ray energetics and mass (CREAM) instrument, *Nucl. Instrum. Methods A* 579 (2007) 1034–1053.
- [37] P. Maestro et al., Energy cross-calibration from the first CREAM flight: transition radiation detector versus calorimeter, in: *Proceedings 30th International Cosmic Ray Conference*, vol. 2, 2007, pp. 333–336.
- [38] O. Ganel et al., Beam tests of the balloon-borne ATIC experiment, *Nucl. Instrum. Methods A* 552/3 (2005) 409–419.
- [39] M. Ave et al., Propagation and source energy spectra of cosmic ray nuclei at high energies, *Astrophys. J.* 697 (2009) 106–114.
- [40] H.S. Ahn et al., the CREAM collaboration, Discrepant hardening observed in cosmic-ray elemental spectra, *Astrophys. J. Lett.* 714 (2010) L89–L92.
- [41] O. Adriani et al., PAMELA measurements of cosmic-ray proton and helium spectra, *Science* 332 (2011) 69–76.
- [42] Y.S. Yoon et al., Cosmic-ray proton and helium spectra from the first CREAM flight, *Astrophys. J.* 728 (2011) 122–129.
- [43] M.J. Ryan et al., Cosmic ray proton and helium spectra above 50 GeV, *Phys. Rev. Lett.* 28 (1972) 985–988.
- [44] Y. Ohira, K. Ioka, Cosmic-ray helium hardening, *Astrophys. J. Lett.* 729 (2011) L13–L17.
- [45] P. Blasi, E. Amato, Diffusive propagation of cosmic rays from supernova remnants in the Galaxy. I: spectrum and chemical composition, 2011, <arXiv:1105.4521[astro-ph]>.
- [46] A. Abdo et al., Discovery of localized region of excess 10-TeV cosmic rays, *Phys. Rev. Lett.* 101 (2008) 221101.
- [47] E.S. Seo et al., Measurement of cosmic ray proton and helium spectra during the 1987 solar minimum, *Astrophys. J.* 378 (1991) 763–772.
- [48] G.V. Kulikov, G.B. Kristiansen, On the size spectrum of extensive air showers, *J. Exp. Theor. Phys.* 35 (1958) 635.
- [49] A. Obermeier, A direct measurement of cosmic rays to very high energies, Doctoral Thesis, Radboud Universiteit Nijmegen, Germany, 2011.
- [50] J.S. George et al., Elemental composition and energy spectra of galactic cosmic rays during solar cycle 23, *Astrophys. J.* 698 (2009) 1666–1681.
- [51] C.J. Cesarsky, Cosmic-ray confinement in the Galaxy, *Ann. Rev. Astron. Astrophys.* 18 (1980) 289–319.
- [52] E.S. Seo, V.S. Ptuskin, Stochastic reacceleration of cosmic rays in the interstellar medium, *Astrophys. J.* 431 (1994) 705–714.
- [53] S.P. Swordy, D. Muller, P. Meyer, J. L'Heureux, J.M. Grunsfeld, Relative abundances of secondary and primary cosmic rays at high energies, *Astrophys. J.* 349 (1990) 625–633.
- [54] E.G. Berezhko et al., Cosmic ray production in supernova remnants including reacceleration: The secondary to primary ratio, *Astron. Astrophys.* 410 (2003) 189–198.
- [55] H.S. Ahn et al., the CREAM collaboration, Measurements of the relative abundances of high-energy cosmic-ray nuclei in the TeV/nucleon region, *Astrophys. J.* 715 (2010) 1400–1407.
- [56] M. Cass'è, P. Goret, Ionization models of cosmic ray sources, *Astrophys. J.* 221 (1978) 703–712.
- [57] B.F. Rauch et al., “Cosmic ray origin in OB associations and preferential acceleration of refractory elements: evidence from abundances of elements  $^{26}\text{Fe}$  through  $^{34}\text{Se}$ ”, *Astrophys. J.* 697 (2009) 2083–2088.
- [58] J.C. Higdon, R.E. Lingenfelter, The superbubble origin of  $^{22}\text{Ne}$  in cosmic rays, *Astrophys. J.* 590 (2003) 822–832.
- [59] S.E. Woosley, A. Heger, Nucleosynthesis and remnants in massive stars of solar metallicity, *Phys. Rep.* 442 (2007) 269–283.
- [60] D.C. Ellison, L. O'C. Drury, J.-P. Meyer, Galactic cosmic rays from supernova remnants. II. Shock acceleration of gas and dust, *Astrophys. J.* 487 (1997) 197–217.
- [61] J.C. Higdon, R.E. Lingenfelter, R. Ramaty, Cosmic-ray acceleration from supernova ejecta in superbubbles, *Astrophys. J.* 509 (1998) L33.
- [62] G.A. deNolfo et al., Identifying galactic cosmic ray origins with super-TIGER, in: *Proceedings 31st International Cosmic Ray Conference*, 2009, p. 1100.
- [63] K. Greisen, End to the cosmic-ray spectrum?, *Phys. Rev. Lett.* 16 (1966) 748–750.
- [64] G.T. Zatsepin, V.A. Kuz'min, Upper limit of the spectrum of cosmic rays, *J. Exp. Theor. Phys. Lett.* 4 (1966) 78–80.
- [65] A. Haungs et al., Latest results and perspectives of the KASCADE-grande EAS facility, *Nucl. Instrum. Methods A* 662 (2012) S150–S156.
- [66] G. Aielli et al., Mean interplanetary magnetic field measurement using the ARGO-YBJ experiment, *Astrophys. J.* 729 (2011) 113–116.
- [67] S. Ostapchenko, Status of QGSJET, in: *C2CR07 – Colliders to Cosmic rays AIP Conference Proceedings*, vol. 928, 2007, pp. 118–125.
- [68] E.J. Ahn et al., Cosmic ray interaction event generator SIBYLL 2.1, *Phys. Rev. D* 80 (2009) 094003.
- [69] P.W. Gorham et al., Observational constraints on the ultrahigh energy cosmic neutrino flux from the second flight of the ANITA experiment, *Phys. Rev. D* 82 (2010) 022004.
- [70] S. Hoover et al., Observation of ultrahigh-energy cosmic rays with the ANITA balloon-borne radio interferometer, *Phys. Rev. Lett.* 105 (2010) 51101.
- [71] M. Ichimura et al., Observation of heavy cosmic-ray primaries over the wide energy range from  $\sim 100$  GeV/particle to  $\sim 100$  TeV/particle: is the celebrated “knee” actually so prominent?, *Phys. Rev. D* 48 (1993) 1949–1975.
- [72] I.P. Ivanenko et al., Energy spectra of cosmic rays above 2 TeV as measured by the “SOKOL” apparatus, in: *Proceedings 23rd International Cosmic Ray Conference*, vol. 2, 1993, pp. 17–20.
- [73] I. Cholis et al., Case for a 700 + GeV WIMP: cosmic ray spectra from PAMELA, Fermi, and ATIC, *Phys. Rev. D* 80 (2009) 123518.
- [74] P.L. Biermann, Cosmic rays. 1. The cosmic ray spectrum between  $10^4$  GeV and  $3 \times 10^9$  GeV, *Astron. Astrophys.* 271 (1993) 649–658.
- [75] P.L. Biermann et al., The origin of cosmic rays: explosions of massive stars with magnetic winds and their supernova mechanism, *Astrophys. J.* 725 (2010) 184–187.
- [76] M. Hillas, Can diffusive shock acceleration in supernova remnants account for high-energy galactic cosmic rays?, *J. Phys. G Nucl. Part. Phys.* 31 (2005) R95–R131.

- [77] D.C. Ellison, E.G. Berezhko, M.G. Baring, Nonlinear shock acceleration and photon emission in supernova remnants, *Astrophys. J.* 540 (2000) 292–307.
- [78] G.E. Allen, J.C. Houck, S.J. Sturmer, Evidence of a curved synchrotron spectrum in the supernova remnant SN 1006, *Astrophys. J.* 683 (2008) 773–785.
- [79] D. Erlykin, A.W. Wolfendale, ‘Fine structure’ in the energy spectrum, and changes in the mass composition of cosmic rays in the energy range 0.3–10 PeV, *Astron. Astrophys.* 350 (1999) L1–L4.
- [80] V.I. Zatsepin, N.V. Sokolskaya, Three component model of cosmic ray spectra from 10 GeV to 100 PeV, *Astron. Astrophys.* 458 (2006) 1–5.
- [81] V.S. Ptuskin et al., Spectrum of galactic cosmic rays accelerated in supernova remnants, *Astrophys. J.* 718 (2010) 31–36.
- [82] G.A. Medina-Tanco, R. Opher, Spatial and temporal distributed acceleration of cosmic rays by supernova remnants three-dimensional simulations, *Astrophys. J.* 411 (1993) 690–707.
- [83] F. Donato, P.D. Serpico, “Discrepant hardenings” in cosmic ray spectra: a first estimate of the effects on secondary antiproton and diffuse gamma-ray yields, *Phys. Rev. D.* 83 (2011) 023014.
- [84] R. Taillet, D. Maurin, Spatial origin of galactic cosmic rays in diffusion models – I. Standard sources in the galactic disk, *Astron. Astrophys.* 402 (2003) 971–983.
- [85] J. Lavalle, Impact of the spectral hardening of TeV cosmic rays on the prediction of the secondary positron flux, *Mon. Not. Roy. Astron. Soc.* 414 (2011) 985–994.